

# Two-dimensional halide perovskite lateral epitaxial heterostructures

<https://doi.org/10.1038/s41586-020-2219-7>

Received: 14 August 2019

Accepted: 10 February 2020

Published online: 29 April 2020

 Check for updates

Enzheng Shi<sup>1,9</sup>, Biao Yuan<sup>2,9</sup>, Stephen B. Shirling<sup>1</sup>, Yao Gao<sup>1</sup>, Akriti<sup>1</sup>, Yunfan Guo<sup>3</sup>, Cong Su<sup>4</sup>, Minliang Lai<sup>5</sup>, Peidong Yang<sup>5,6,7</sup>, Jing Kong<sup>3</sup>, Brett M. Savoie<sup>1,✉</sup>, Yi Yu<sup>2,✉</sup> & Letian Dou<sup>1,✉</sup>

Epitaxial heterostructures based on oxide perovskites and III–V, II–VI and transition metal dichalcogenide semiconductors form the foundation of modern electronics and optoelectronics<sup>1–7</sup>. Halide perovskites—an emerging family of tunable semiconductors with desirable properties—are attractive for applications such as solution-processed solar cells, light-emitting diodes, detectors and lasers<sup>8–15</sup>. Their inherently soft crystal lattice allows greater tolerance to lattice mismatch, making them promising for heterostructure formation and semiconductor integration<sup>16,17</sup>. Atomically sharp epitaxial interfaces are necessary to improve performance and for device miniaturization. However, epitaxial growth of atomically sharp heterostructures of halide perovskites has not yet been achieved, owing to their high intrinsic ion mobility, which leads to interdiffusion and large junction widths<sup>18–21</sup>, and owing to their poor chemical stability, which leads to decomposition of prior layers during the fabrication of subsequent layers. Therefore, understanding the origins of this instability and identifying effective approaches to suppress ion diffusion are of great importance<sup>22–26</sup>. Here we report an effective strategy to substantially inhibit in-plane ion diffusion in two-dimensional halide perovskites by incorporating rigid π-conjugated organic ligands. We demonstrate highly stable and tunable lateral epitaxial heterostructures, multiheterostructures and superlattices. Near-atomically sharp interfaces and epitaxial growth are revealed by low-dose aberration-corrected high-resolution transmission electron microscopy. Molecular dynamics simulations confirm the reduced heterostructure disorder and larger vacancy formation energies of the two-dimensional perovskites in the presence of conjugated ligands. These findings provide insights into the immobilization and stabilization of halide perovskite semiconductors and demonstrate a materials platform for complex and molecularly thin superlattices, devices and integrated circuits.

Two-dimensional (2D) halide perovskites exhibit high photoluminescence quantum yield, long carrier lifetime and diffusion length, and remarkable optoelectronic tunability, owing to their structural and compositional flexibility<sup>27–34</sup>. These 2D perovskites form quantum wells composed of periodically repeating organic and inorganic layers along the out-of-plane direction, providing further structure and property tunability<sup>35,36</sup>. In this work, the synthesis of 2D halide perovskite lateral heterostructures is performed via a solution-phase sequential growth approach, as shown in Supplementary Fig. 1. In general, halide perovskites are susceptible to damage after two or more sequential growth steps, particularly when subsequent growth is performed in more aggressive conditions than the prior step—for example, under a higher temperature or using a more polar solvent. To eliminate the possibility of damaging the existing crystals, subsequent growth is

performed under relatively milder growth conditions, such as lowering the growth temperature or adding more antisolvent in the precursor solution. Thus, subsequent halide perovskites are nucleated along the edges of the prior 2D crystals, thereafter forming concentric square/rectangular 2D lateral heterostructures directly on the SiO<sub>2</sub>/Si substrate. By controlling the solution concentration and the growth temperature and time, the lateral size and vertical thickness of the 2D crystal can be controlled (Supplementary Figs. 2–4).

## Lateral heterostructure formation

As shown in Fig. 1a, b, we create two types of lateral 2D halide perovskite heterostructures using different organic ligands: a conjugated ligand based on bithiophenylethylammonium (2T<sup>+</sup>; Fig. 1a and Supplementary

<sup>1</sup>Davidson School of Chemical Engineering, Purdue University, West Lafayette, IN, USA. <sup>2</sup>School of Physical Science and Technology, ShanghaiTech University, Shanghai, China. <sup>3</sup>Department of Electrical Engineering and Computer Science, Massachusetts Institute of Technology, Cambridge, MA, USA. <sup>4</sup>Research Lab of Electronics (RLE), Massachusetts Institutes of Technology, Cambridge, MA, USA. <sup>5</sup>Department of Chemistry, University of California, Berkeley, CA, USA. <sup>6</sup>Materials Sciences Division, Lawrence Berkeley National Laboratory, Berkeley, CA, USA. <sup>7</sup>Kavli Energy NanoScience Institute, Berkeley, CA, USA. <sup>8</sup>Birck Nanotechnology Center, Purdue University, West Lafayette, IN, USA. <sup>9</sup>These authors contributed equally: Enzheng Shi, Biao Yuan.  
✉e-mail: bsavoie@purdue.edu; yuy1@shanghaitech.edu.cn; dou10@purdue.edu

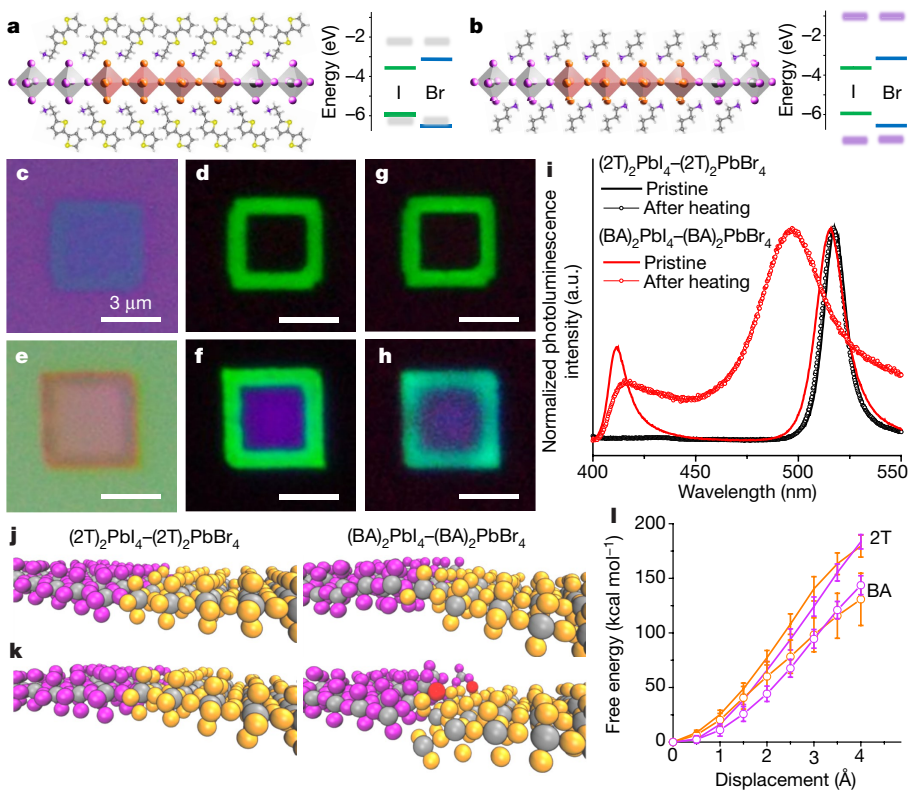


**Fig. 1 | 2D halide perovskite lateral heterostructures stabilized by conjugated ligands.** **a, b**, Schematic illustrations and proposed band alignments of  $(2T)_2\text{PbI}_4$ – $(2T)_2\text{PbBr}_4$  (**a**) and  $(\text{BA})_2\text{PbI}_4$ – $(\text{BA})_2\text{PbBr}_4$  (**b**) lateral heterostructures. The pairs of blue and green lines in the band diagrams at right represent the conduction band minimum and valence band maximum of inorganic  $[\text{PbBr}_4]^{2-}$  and  $[\text{PbI}_4]^{2-}$  octahedral layers, respectively. The broad, semi-transparent pairs of grey and purple lines correspond to the highest occupied molecular orbital and lowest unoccupied molecular orbital levels of the  $2T^+$  and  $\text{BA}^+$  organic layers, respectively. **c, d**, Optical (**c**) and photoluminescence (**d**) images of a  $(2T)_2\text{PbI}_4$ – $(2T)_2\text{PbBr}_4$  lateral heterostructure. **e, f**, Optical (**e**) and photoluminescence (**f**) images of a  $(\text{BA})_2\text{PbI}_4$ – $(\text{BA})_2\text{PbBr}_4$  lateral heterostructure. **g**, Photoluminescence image of the  $(2T)_2\text{PbI}_4$ – $(2T)_2\text{PbBr}_4$  lateral heterostructure after 1 h of heating at 100 °C. All scale bars are 3 μm. **h**, Photoluminescence image of the  $(\text{BA})_2\text{PbI}_4$ – $(\text{BA})_2\text{PbBr}_4$  lateral heterostructure after 1 h of heating at 100 °C. All scale bars are 3 μm. **i**, Corresponding photoluminescence spectra of the heterostructures before and after heating. **j, k**, Snapshots from the molecular dynamics simulations at 298 K (**j**) and 800 K (**k**) for  $(2T)_2\text{PbI}_4$ – $(2T)_2\text{PbBr}_4$  (left) and  $(\text{BA})_2\text{PbI}_4$ – $(\text{BA})_2\text{PbBr}_4$  (right) showing the interface between each perovskite domain. For clarity, the organic ligands have been omitted. The colours correspond to: purple, iodine atoms; orange, bromine atoms; grey, lead atoms. In  $(\text{BA})_2\text{PbI}_4$ – $(\text{BA})_2\text{PbBr}_4$ , the iodine atoms that have diffused across the interface and into the bromine domain are indicated in red. **l**, Free energy for removing a halide atom from an apical position to vacuum to generate a halide vacancy. The orange plots correspond to bromide perovskite and purple plots correspond to iodide perovskites. a.u., arbitrary units.

Table 1) and a widely studied alkyl ligand, butylammonium ( $\text{BA}^+$ ; Fig. 1b). The heterostructures exhibit two concentric regions with slight optical contrast and distinct photoluminescence emissions, including the central square/rectangular bromide region and the peripheral iodide region with a uniform width of about 1–2 μm for the iodide region (Fig. 1c–f). For  $(2T)_2\text{PbI}_4$ – $(2T)_2\text{PbBr}_4$  heterostructures, no photoluminescence emission is detected from the central  $(2T)_2\text{PbBr}_4$  region, which is attributed to type-II band alignment between the inorganic  $[\text{PbBr}_4]^{2-}$  and organic ligand  $2T^+$  layers as shown in the proposed band alignment (Fig. 1a)<sup>37</sup>.  $(2T)_2\text{PbI}_4$  has a green photoluminescence emission (Fig. 1d, i) that peaks at 515 nm from the type-I band alignment between the  $[\text{PbI}_4]^{2-}$  and  $2T^+$  layers (Fig. 1a). The creation of the  $(\text{BA})_2\text{PbI}_4$ – $(\text{BA})_2\text{PbBr}_4$  heterostructure follows a similar synthetic procedure (Fig. 1e, f). It is known that the Br–I heterostructure is not thermally stable in three-dimensional perovskites because of the large solid-state diffusivity of  $\text{Br}^-$  and  $\text{I}^-$ . Interdiffusion of halide anions across the heterojunction can be triggered and accelerated upon mild heating<sup>20,21</sup>. Here, however, we found that when the conjugated 2T ligands are used, the interdiffusion between  $\text{Br}^-$  and  $\text{I}^-$  in the  $(2T)_2\text{PbI}_4$ – $(2T)_2\text{PbBr}_4$  heterostructure is substantially inhibited. As shown in Fig. 1g, after heating at 100 °C for 1 h, no difference is observed in the photoluminescence image, and the photoluminescence emission shift is within 1 nm (Fig. 1i, with extended temperatures and times

**h**, Photoluminescence image of the  $(\text{BA})_2\text{PbI}_4$ – $(\text{BA})_2\text{PbBr}_4$  lateral heterostructure after 1 h of heating at 100 °C. All scale bars are 3 μm. **i**, Corresponding photoluminescence spectra of the heterostructures before and after heating. **j, k**, Snapshots from the molecular dynamics simulations at 298 K (**j**) and 800 K (**k**) for  $(2T)_2\text{PbI}_4$ – $(2T)_2\text{PbBr}_4$  (left) and  $(\text{BA})_2\text{PbI}_4$ – $(\text{BA})_2\text{PbBr}_4$  (right) showing the interface between each perovskite domain. For clarity, the organic ligands have been omitted. The colours correspond to: purple, iodine atoms; orange, bromine atoms; grey, lead atoms. In  $(\text{BA})_2\text{PbI}_4$ – $(\text{BA})_2\text{PbBr}_4$ , the iodine atoms that have diffused across the interface and into the bromine domain are indicated in red. **l**, Free energy for removing a halide atom from an apical position to vacuum to generate a halide vacancy. The orange plots correspond to bromide perovskite and purple plots correspond to iodide perovskites. a.u., arbitrary units.

in Supplementary Fig. 5), suggesting negligible halide interdiffusion across the  $(2T)_2\text{PbI}_4$ – $(2T)_2\text{PbBr}_4$  interface. By contrast, halide interdiffusion is fast in the reference heterostructure  $(\text{BA})_2\text{PbI}_4$ – $(\text{BA})_2\text{PbBr}_4$ . As shown in Fig. 1h, i, after 1 h of heating at 100 °C, the interface between the blue region associated with  $(\text{BA})_2\text{PbBr}_4$  and the green region associated with  $(\text{BA})_2\text{PbI}_4$  becomes blurry, and there is a drastic change in the photoluminescence emission spectrum (extended temperatures and times are presented in Supplementary Fig. 6). The green peak initially located at 515 nm blueshifts to 496 nm, whereas the blue peak redshifts from 411 nm to 415 nm. Meanwhile, the peaks become much broader, indicating pronounced I/Br interdiffusion and alloying. It is estimated that the diffusion is slowed down by two to three orders of magnitude in the 2T heterostructures compared to the BA-based heterostructures (Supplementary Fig. 7).

## Stabilization mechanism

Molecular dynamics simulations were used to investigate the suppression of halide interdiffusion in the  $(2T)_2\text{PbI}_4$ – $(2T)_2\text{PbBr}_4$  heterostructure. The simulations on heterostructures of  $(2T)_2\text{PbI}_4$ – $(2T)_2\text{PbBr}_4$  and  $(\text{BA})_2\text{PbI}_4$ – $(\text{BA})_2\text{PbBr}_4$  at both room and elevated temperatures (298 K and 800 K, respectively) are consistent with the experimental observations: for  $(2T)_2\text{PbI}_4$ – $(2T)_2\text{PbBr}_4$ , no diffusion is observed at

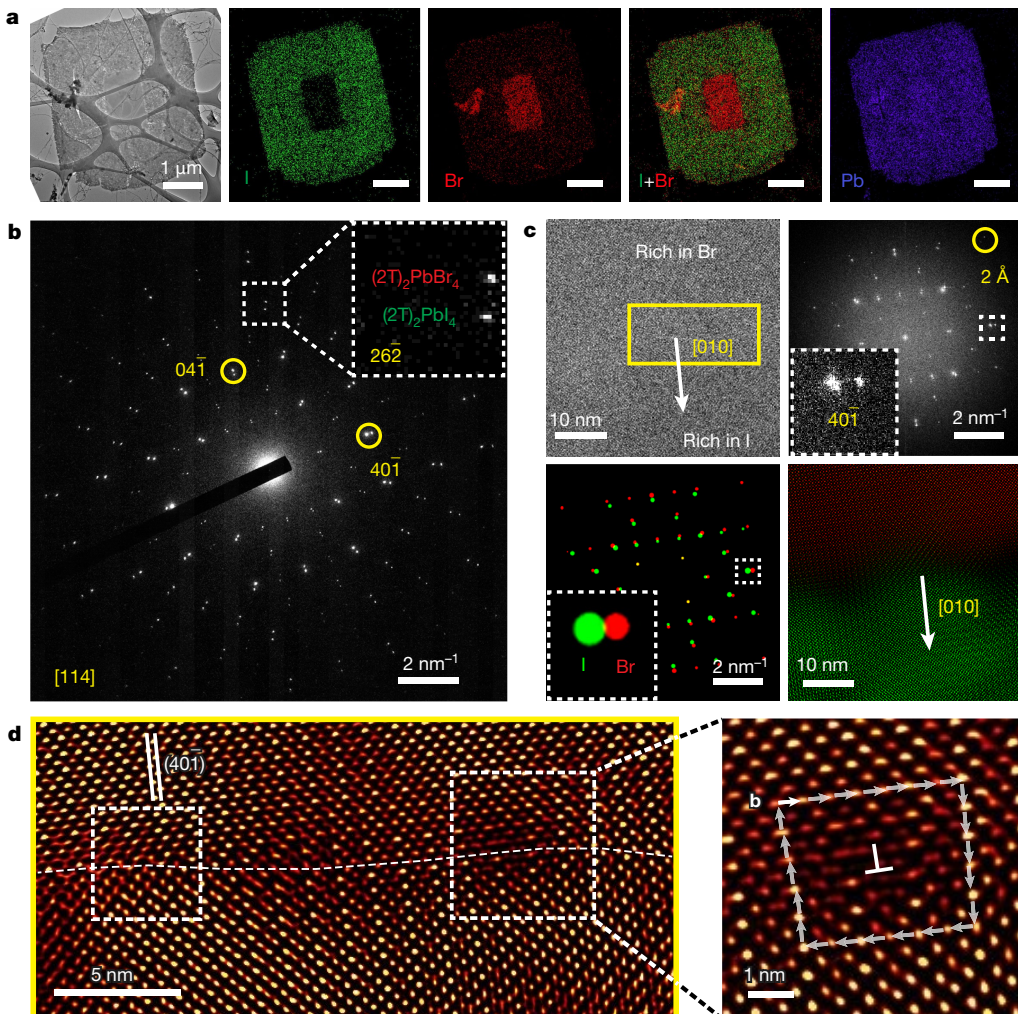


**Fig. 2 | TEM characterization of the  $(2T)_2\text{PbI}_4$ – $(2T)_2\text{PbBr}_4$  heterostructure.** **a**, Low-magnification TEM image (left), followed by EDS elemental mappings of one  $(2T)_2\text{PbI}_4$ – $(2T)_2\text{PbBr}_4$  heterostructure, for (left to right): I, Br, I+Br and Pb. The scale bars are 1  $\mu\text{m}$ . **b**, SAED pattern of the  $(2T)_2\text{PbI}_4$ – $(2T)_2\text{PbBr}_4$  interface. Inset, enlarged view of one pair of splitting diffraction spots, which correspond to the  $(26\bar{2})$  plane. The zone axis is [114]. The  $(04\bar{1})$  and  $(40\bar{1})$  planes are highlighted by yellow circles. **c**, AC-HRTEM and Fourier analysis. Top left, a selected AC-HRTEM image. Top right, Fourier transform pattern of the AC-HRTEM image. One pair of splitting spots is enlarged and shown in the inset, corresponding to the  $(40\bar{1})$  plane in **b**. The outer spot at the top right is

highlighted by a yellow circle; the corresponding lattice distance is 2  $\text{\AA}$ . Bottom left, false-colour Fourier masks for two sets of spots. One pair of masks for splitting spots is enlarged and shown in the inset. Bottom right, corresponding overlap (in false colour) of two sets of lattice fringes from  $(2T)_2\text{PbI}_4$  (green) and  $(2T)_2\text{PbBr}_4$  (red). **d**, Fourier filtered and magnified AC-HRTEM images of the yellow rectangular area in **c** (top left) showing the epitaxial interface. Left, the two solid white lines denote the  $(40\bar{1})$  planes, and the two dashed white boxes highlight edge dislocations. Right, enlarged image of the rightmost highlighted edge dislocation; the bold white arrow denotes the Burgers vector **b**.

either temperature, whereas halide diffusion across the interface is observed in  $(\text{BA})_2\text{PbI}_4$ – $(\text{BA})_2\text{PbBr}_4$  at elevated temperatures. As shown visually in Fig. 1j, k, the amount of disorder at the interface is affected by the choice of organic ligand. In  $(2T)_2\text{PbI}_4$ – $(2T)_2\text{PbBr}_4$ , the interface remains pristine and well ordered at elevated temperature. By contrast, interdiffusion and increased disorder are observed at the  $(\text{BA})_2\text{PbI}_4$ – $(\text{BA})_2\text{PbBr}_4$  heterojunction at elevated temperature. As comparative measures of the disorder, the displacements of the lead atoms from the 2D perovskite plane and octahedral tilt angles were summarized from the simulations (Supplementary Fig. 8). The displacements for  $(2T)_2\text{PbI}_4$ – $(2T)_2\text{PbBr}_4$  are less than around 2  $\text{\AA}$  at both room and elevated temperatures; by contrast,  $(\text{BA})_2\text{PbI}_4$ – $(\text{BA})_2\text{PbBr}_4$  shows displacements >3  $\text{\AA}$  and >4  $\text{\AA}$  at room temperature and elevated temperatures, respectively. Consistent trends are observed in the tilt angle results, with broader distributions occurring in proximity to the heterojunction (Supplementary Fig. 9). The increased disorder at room temperature is also consistent

with the reduced resolution observed for BA-based compounds in the photoluminescence experiments (Supplementary Fig. 6). The larger and more rigid conjugated organic ligands are thus able to stabilize the interface and inorganic framework more effectively, whereas the smaller organic ligand leads to softer inorganic lattice that can accommodate the mismatch in halide sizes and facilitate halide interdiffusion.

Vacancy generation at high temperatures could also influence the interdiffusion process. For a vacancy-mediated diffusion process, the diffusion constant  $D$  can be expressed as<sup>38</sup>

$$D = D_0 \exp\left(-\frac{E_a}{k_B T}\right) = \alpha a^2 \omega N_v$$

$$N_v = \exp\left(-\frac{\Delta G}{k_B T}\right) = \exp\left(\frac{\Delta S}{k_B}\right) \exp\left(-\frac{\Delta H}{k_B T}\right)$$

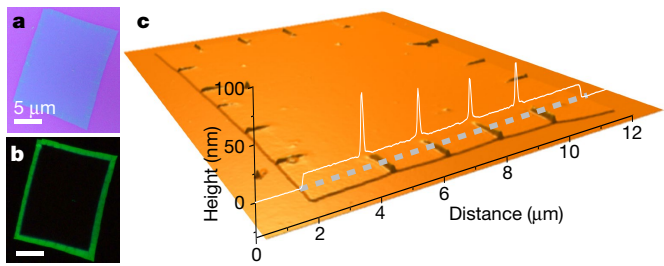


**Fig. 3 | Periodic ripples in  $(2T)_2\text{PbI}_4$ – $(2T)_2\text{PbBr}_4$  lateral heterostructures.** **a, b,** Optical and photoluminescence images of a one-pot  $(2T)_2\text{PbI}_4$ – $(2T)_2\text{PbBr}_4$  lateral heterostructure; ripples in the  $(2T)_2\text{PbI}_4$  region can be distinguished. The scale bars are 5  $\mu\text{m}$ . **c,** AFM image of the one-pot  $(2T)_2\text{PbI}_4$ – $(2T)_2\text{PbBr}_4$  lateral heterostructure with clear ripples. The height profile along the grey dashed line indicates that the height of the ripples is around 40–50 nm.

where  $D_0$  is the pre-exponential factor in the Arrhenius equation,  $E_a$  is the activation energy for the vacancy-assisted ion migration,  $N_v$  is the fraction of vacancies in the solid,  $\alpha$  is a geometric constant,  $a$  is the elementary jump distance,  $\omega$  is the jump frequency,  $k_B$  is the Boltzmann constant,  $T$  is the absolute temperature and  $\Delta H$ ,  $\Delta S$  and  $\Delta G$  are, respectively, the enthalpy change, the entropy change and the change in the Gibbs free energy for the formation of a vacancy. The vacancy concentration  $N_v$  is usually treated as a constant for most oxide materials and  $\omega$  is the only temperature-dependent factor. However, for halide materials, the vacancy formation energy is normally much lower and therefore both  $N_v$  and  $\omega$  are Arrhenius activated. Taking this into consideration, multistate Bennett acceptance ratio calculations on pure 2D perovskite systems were used to investigate halide and ligand vacancy formation (Fig. 1*i*). Using the BA ligand, the activation barrier to generate halide vacancies is much lower than that of the 2T ligand. Meanwhile, the free energy for creating a ligand vacancy by removing a ligand molecule from the surface is similar for both BA and 2T for a given halide species (Supplementary Fig. 10), indicating that the vacancy concentrations for the BA and 2T ligands are similar and may not play a dominant role. From these calculations, the number of ligand vacancies is expected to be similar upon heating the crystals, whereas a greater concentration of halide vacancies is to be expected in  $(\text{BA})_2\text{PbI}_4$ – $(\text{BA})_2\text{PbBr}_4$  heterojunctions, which also promotes faster anion interdiffusion. Therefore, it is suggested that both the lower interfacial disorder and the lower halide vacancy concentration in 2T-based perovskites probably contribute to the inhibition of the halide interdiffusion in the  $(2T)_2\text{PbI}_4$ – $(2T)_2\text{PbBr}_4$  heterojunctions. As suggested by the differences between the free energy calculations for ligand and halide vacancy generation, the differences in the interfacial stability are largely attributed to the identity of the ligands and not to the identity of the individual halides.

## Interface imaging and analysis

Energy dispersive X-ray spectroscopy (EDS) and selected area electron diffraction (SAED) were used to provide structural insights into the ultrathin  $(2T)_2\text{PbI}_4$ – $(2T)_2\text{PbBr}_4$  heterostructures. Because the heterostructures are directly grown on  $\text{SiO}_2/\text{Si}$  substrates, it is challenging to transfer the heterostructures to the TEM grids. To address this issue, we used a sacrificial polymethyl methacrylate (PMMA) layer on the growth substrate before the growth of heterostructures. The growth substrate with the PMMA layer was then soaked in chlorobenzene (see Methods) to release the 2D crystals, facilitating easy transfer of the 2D crystals to the TEM grid. The low-magnification TEM image and EDS elemental mappings of a  $(2T)_2\text{PbI}_4$ – $(2T)_2\text{PbBr}_4$  heterostructure (Fig. 2a) show that Pb is distributed uniformly throughout the heterostructure, whereas I and Br are concentrated in the peripheral

and central regions, respectively. This is consistent with photoluminescence, X-ray diffraction (XRD) and scanning electron microscopy (SEM) characterizations (Fig. 1 and Supplementary Fig. 11). Hybrid perovskites are known to undergo rapid degradation under electron-beam irradiation. To avoid structural damage from the electron beams, the SAED patterns were obtained with a reduced electron dose rate (that is, less than  $0.1 \text{ e } \text{\AA}^{-2} \text{ s}^{-1}$ ;  $e$ , electron). By comparing the experimental diffraction patterns with the kinematical simulated patterns, the zone axis for electron diffraction is determined to be [114] (see Supplementary Fig. 12 and related discussion). As shown in Supplementary Figs. 12, 13, the slight difference in diffraction patterns between pure  $(2T)_2\text{PbI}_4$  and  $(2T)_2\text{PbBr}_4$  sheets is attributed to their lattice mismatch (about 5–6%, Supplementary Tables 2, 3). For the  $(2T)_2\text{PbI}_4$ – $(2T)_2\text{PbBr}_4$  interface, the SAED pattern (Fig. 2b) is composed of two sets of patterns with identical orientation from  $(2T)_2\text{PbI}_4$  and  $(2T)_2\text{PbBr}_4$ , respectively, suggesting the epitaxial growth of  $(2T)_2\text{PbI}_4$  from the  $(2T)_2\text{PbBr}_4$  sheet.

To achieve a higher spatial resolution of the heterostructure interface while minimizing the radiation damage, low-dose aberration-corrected high-resolution transmission electron microscopy (AC-HRTEM) was performed at an accelerating voltage of 80 kV (Fig. 2c, d and Supplementary Fig. 14). In our early work, atomic-resolution imaging was achieved on all inorganic halide perovskites, taking advantage of low-dose AC-HRTEM<sup>39</sup>. Here, further incorporated with a minimum-dose strategy (Supplementary Fig. 14), the lattice information of radiation-sensitive hybrid organic–inorganic halide perovskites was successfully revealed. The continuous lattice fringes can be imaged at the  $(2T)_2\text{PbI}_4$ – $(2T)_2\text{PbBr}_4$  interface (Fig. 2c, top left), and its corresponding Fourier transform information (Fig. 2c, top right) is consistent with the SAED pattern (Fig. 2b), further confirming the epitaxial growth between  $(2T)_2\text{PbBr}_4$  and  $(2T)_2\text{PbI}_4$  at the nanometre scale. A Fourier filtering technique was also used to further resolve the interface. Owing to the different lattice constants between the two segments across the interface, the real-space lattice information is obtained by applying well tuned masks in Fourier space. The masked green and red areas in Fig. 2c (bottom left) correspond to the lattice information from  $(2T)_2\text{PbI}_4$  (Supplementary Fig. 15b) and  $(2T)_2\text{PbBr}_4$  (Supplementary Fig. 15c), respectively. By superimposing the two inverse Fourier transform images, the near-atomically sharp interface can be better distinguished (Fig. 2c, bottom right). The clear interface is also observed in the strain mapping in Supplementary Fig. 16. Geometric phase images demonstrate the near-uniform lattice of the  $(2T)_2\text{PbBr}_4$  layer and periodic lattice deformation of the epitaxial  $(2T)_2\text{PbI}_4$  layer (Supplementary Fig. 16h). To relax the accumulated interfacial strain and stabilize the heteroepitaxy, periodic interfacial misfit dislocations are expected<sup>40</sup>. This is evidenced by our direct observations from the Fourier filtered AC-HRTEM images (Fig. 2d and Supplementary Fig. 17). Figure 2d clearly shows a misfit edge dislocation at the atomic level. In addition to the continuous lattice fringe along the  $(40\bar{1})$  plane on both sides of the interface, the edge dislocations appear at around 15 nm intervals (Supplementary Fig. 17c). Furthermore, by analysing multiple samples, it was found that the  $(2T)_2\text{PbI}_4$  preferentially grew along two directions: [100] and [010] (Supplementary Fig. 18). These observations suggest that the stable heteroepitaxy (Supplementary Fig. 19) between two similar perovskite structures is in-plane connected along the [100] and [010] directions with interfacial strain relaxed by misfit dislocations. The out-of-plane strain is probably relaxed through rearrangement of the organic cations.

In addition to forming misfit dislocations, strain can also be relaxed through ripple formation<sup>7</sup>. Here, we show that such ripples can be observed in the halide perovskite heterostructures. By simply mixing the precursors of  $(2T)_2\text{PbI}_4$  and  $(2T)_2\text{PbBr}_4$ , one-pot synthesis of  $(2T)_2\text{PbI}_4$ – $(2T)_2\text{PbBr}_4$  lateral heterostructures is achieved with a slightly less sharp interface (Fig. 3). The spontaneous formation of  $(2T)_2\text{PbI}_4$ – $(2T)_2\text{PbBr}_4$  lateral heterostructures via the one-pot route is attributed to the large solubility difference between these two compounds (which leads to sequential precipitation from the solution during the solvent evaporation process) and the reduced nucleation

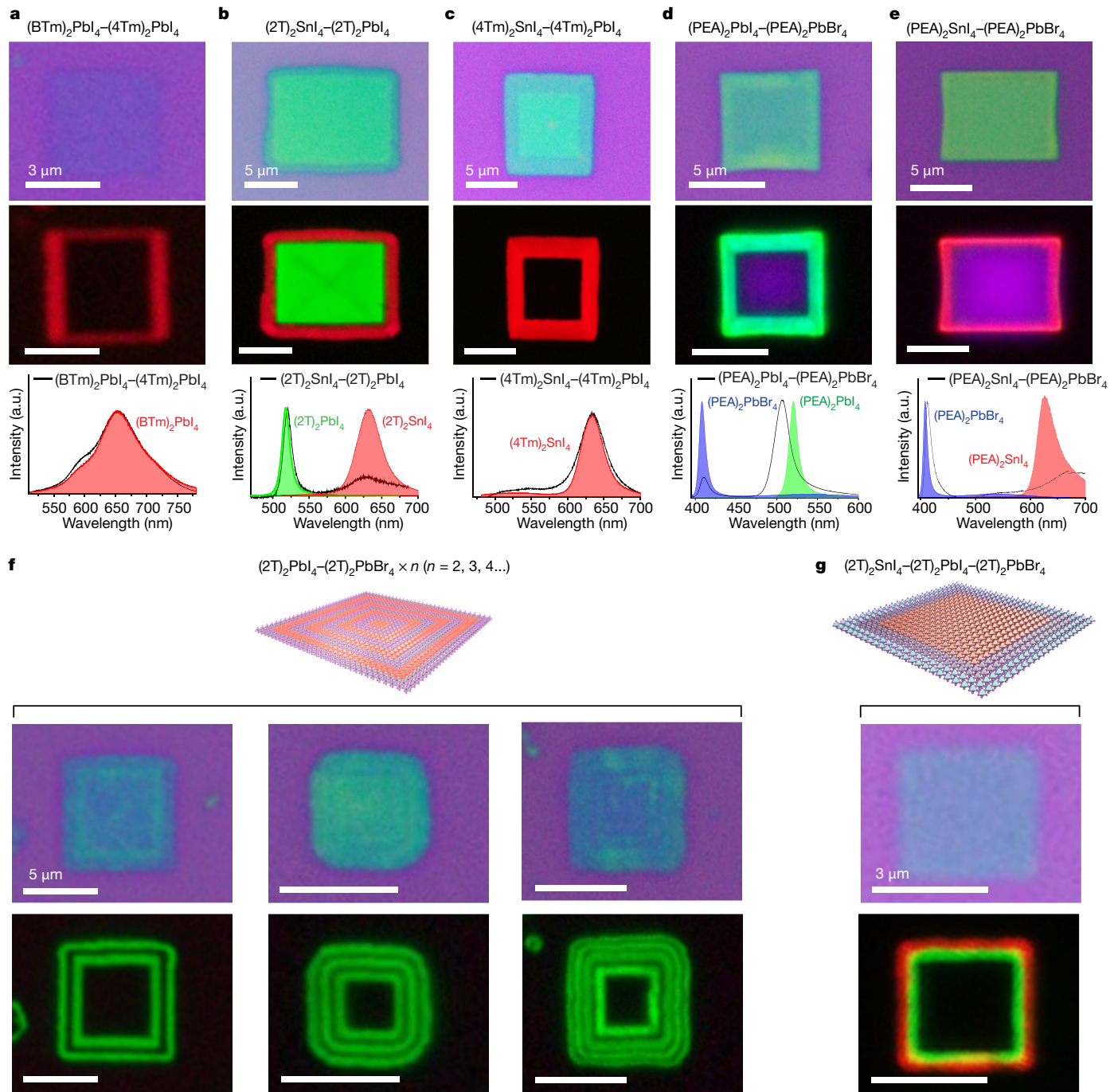


**Fig. 4 | The library of 2D halide perovskite lateral heterostructures, multiheterostructures and superlattices.** **a–e**, Lateral heterostructures of  $(\text{BTm})_2\text{PbI}_4-(4\text{Tm})_2\text{PbI}_4$  (**a**),  $(2\text{T})_2\text{SnI}_4-(2\text{T})_2\text{PbI}_4$  (**b**),  $(4\text{Tm})_2\text{SnI}_4-(4\text{Tm})_2\text{PbI}_4$  (**c**),  $(\text{PEA})_2\text{PbI}_4-(\text{PEA})_2\text{PbBr}_4$  (**d**) and  $(\text{PEA})_2\text{SnI}_4-(\text{PEA})_2\text{PbBr}_4$  (**e**). Top, optical images; middle, photoluminescence images; bottom, photoluminescence

spectra. **f,g**, Schematic illustrations of the  $(2\text{T})_2\text{PbI}_4-(2\text{T})_2\text{PbBr}_4 \times n$  lateral superlattice (**f**; left to right,  $n=2, n=3, n=4$ ) and  $(2\text{T})_2\text{SnI}_4-(2\text{T})_2\text{PbI}_4-(2\text{T})_2\text{PbBr}_4$  lateral multiheterostructure (**g**). Top images are optical and bottom images are photoluminescence. Scale bars for **a** and **g** are 3  $\mu\text{m}$ , all other scale bars are 5  $\mu\text{m}$ .

energy of  $(2\text{T})_2\text{PbI}_4$  along the edge of  $(2\text{T})_2\text{PbBr}_4$  (see Supplementary Figs. 20, 21 and related discussions). In the  $(2\text{T})_2\text{PbI}_4$  regions in these heterostructures, periodic ripples formed—an indication of a coherent interface free of dislocations. From the atomic force microscopy (AFM) image of the heterostructure, the height of the ripples was found to be around 40–50 nm and the inter-distance between adjacent ripples is about 1.6  $\mu\text{m}$ , which agrees with the 5–6% lattice strain. These ripple structures are larger and less dense than those observed in  $\text{WS}_2-\text{WSe}_2$  heterostructures (about 1–2 nm high, approximately every 30 nm)<sup>7</sup>; it is surprising that the weak and soft halide perovskite lattice is able to

preserve the coherency at the heterointerface so well. Lateral interface engineering—including the interfacial dislocations and ripples discovered in 2D halide perovskite heterostructures—provides insights into and opportunities to better control the interface integrity and associated electronic and optoelectronic properties.

### Multicomplex heterostructure formation

We further demonstrate the general synthesis of various lateral heterostructures (between different halides, metal cations and

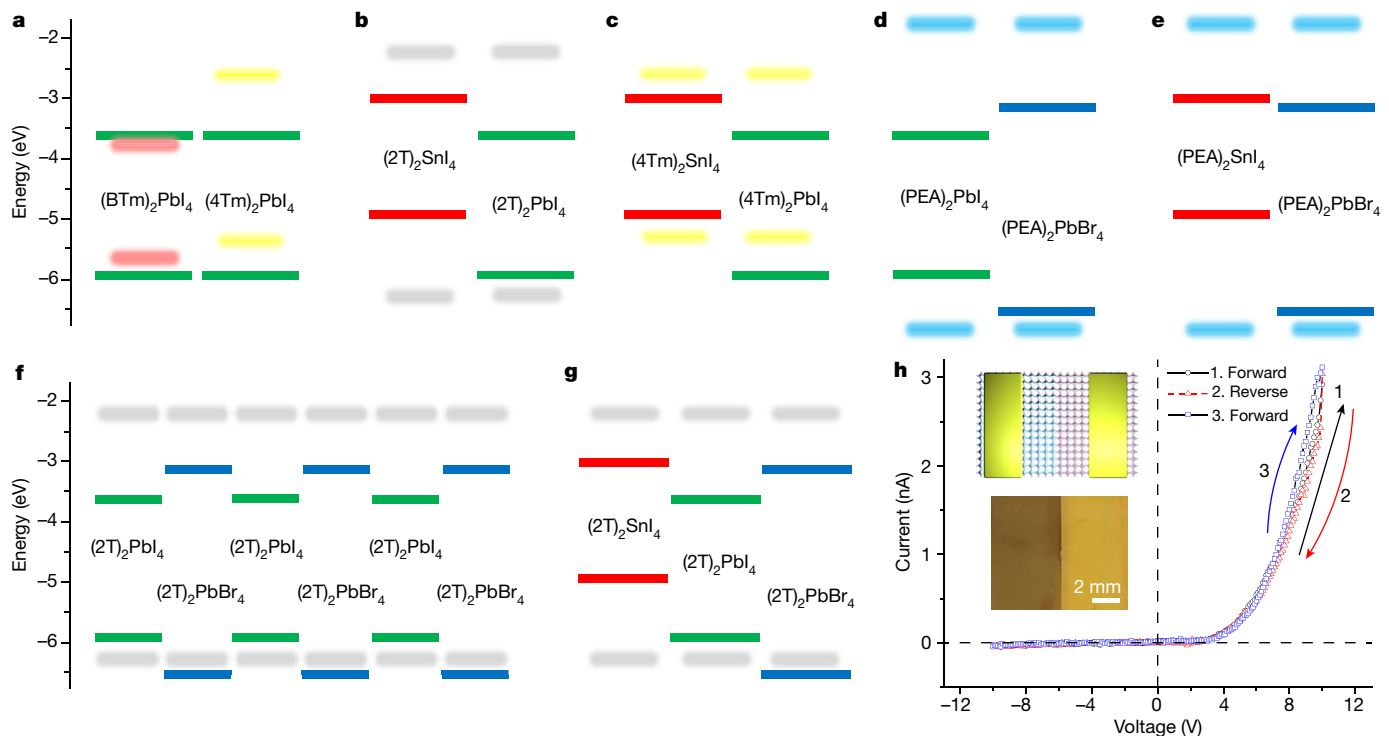


**Fig. 5 | Proposed band alignments and electrical characteristics of the heterostructures.** **a–g**, Proposed band alignments for  $(BTm)_2PbI_4$ – $(4Tm)_2PbI_4$  (**a**),  $(2T)_2SnI_4$ – $(2T)_2PbI_4$  (**b**),  $(4Tm)_2SnI_4$ – $(4Tm)_2PbI_4$  (**c**),  $(PEA)_2PbI_4$ – $(PEA)_2PbBr_4$  (**d**),  $(PEA)_2SnI_4$ – $(PEA)_2PbBr_4$  (**e**),  $(2T)_2PbI_4$ – $(2T)_2PbBr_4$   $\times 3$  superlattice (**f**) and  $(2T)_2SnI_4$ – $(2T)_2PbI_4$ – $(2T)_2PbBr_4$  (**g**). The pairs of blue, green and red lines represent the conduction band minimums and valence band maximums of inorganic  $[PbBr_4]^{2-}$ ,  $[PbI_4]^{2-}$  and  $[SnI_4]^{2-}$  octahedral layers, respectively. The pairs of broad, semi-transparent grey, red, yellow and blue

lines correspond to the highest occupied molecular orbitals and lowest unoccupied molecular orbitals of the  $2T^+$ ,  $BTm^+$ ,  $4Tm^+$  and  $PEA^+$  organic layers, respectively. Band bending and Fermi level matching is not considered as these values have not yet been reliably measured and reported. **h**, Rectification behaviour of a  $(4Tm)_2SnI_4$ – $(4Tm)_2PbI_4$  heterostructure diode device. The labels 1, 2, and 3 denote the current–voltage scan direction and order. Inset, schematic illustration and optical image of the thin-film  $(4Tm)_2SnI_4$ – $(4Tm)_2PbI_4$  heterostructure.

organic ligands) and even superlattices of 2D halide perovskites following the solution-phase epitaxial growth strategy. Additional  $\pi$ -conjugated organic ligands, including phenylethylammonium ( $PEA^+$ ), quaterthiophenylethylammonium ( $4Tm^+$ ) and 7-(thiophen-2-yl)benzothiadiazol-4-yl)-[2,2'-bithiophen]-5-yl)ethylammonium ( $BTm^+$ ), were used. The chemical structures of all ligands in this study are listed in Supplementary Fig. 22a. Corresponding optical and photoluminescence images of each type of 2D sheet are shown in Supplementary Fig. 22b–k. The XRD patterns and photoluminescence spectra of these 2D sheets are summarized in Supplementary Fig. 23. Using these ligands, we synthesized a  $(BTm)_2PbI_4$ – $(4Tm)_2PbI_4$  heterostructure between different organic ligands,  $(2T)_2SnI_4$ – $(2T)_2PbI_4$  and  $(4Tm)_2SnI_4$ – $(4Tm)_2PbI_4$  heterostructures between different metal cations, a  $(PEA)_2PbI_4$ – $(PEA)_2PbBr_4$  heterostructure between different halides, a  $(PEA)_2SnI_4$ – $(PEA)_2PbBr_4$  heterostructure between different halides and metals,  $(2T)_2PbI_4$ – $(2T)_2PbBr_4$   $\times n$  ( $n = 2, 3, 4$ ) superlattices and  $(2T)_2SnI_4$ – $(2T)_2PbBr_4$  multiheterostructures (Fig. 4).

As shown in Fig. 4a, lateral heterostructures can be created between two segments with the distinct organic ligands  $4Tm^+$  and  $BTm^+$  (we note that the sizes for two different organic ligands should be similar to reduce strain). The  $(4Tm)_2PbI_4$  region shows no photoluminescence emission, owing to the type-II band alignment between the  $4Tm^+$  ligand and the  $[PbI_4]^{2-}$  layers (Supplementary Figs. 22f, 23)<sup>41</sup>. The broad red photoluminescence emission from the peripheral region of the heterostructure originates from  $(BTm)_2PbI_4$ , which is attributed to the type-I band alignment between the  $[PbI_4]^{2-}$  layer and the  $BTm^+$  layer (Supplementary Figs. 22g, 23). In addition, the bandgap and optoelectronic properties of the halide perovskite materials can be modulated by altering the metal atoms centring the  $[MX_4]^{2-}$  octahedrons. By substituting

$Pb$  with  $Sn$ , 2D halide perovskite sheets were successfully synthesized with  $2T^+$  and  $4Tm^+$  ligands, including  $(2T)_2SnI_4$  and  $(4Tm)_2SnI_4$  (Supplementary Figs. 22h, i). In combination with the  $Pb$ -based perovskites, both  $(2T)_2SnI_4$ – $(2T)_2PbI_4$  and  $(4Tm)_2SnI_4$ – $(4Tm)_2PbI_4$  lateral heterostructures were created (Fig. 4b, c). Two distinct photoluminescence emission peaks from the  $(2T)_2SnI_4$ – $(2T)_2PbI_4$  heterostructure correspond to pure  $(2T)_2SnI_4$  and  $(2T)_2PbI_4$ , and the gap in the photoluminescence image between the  $Pb$  and  $Sn$  perovskite segments is probably induced by exciton dissociation at the interface. Similarly,  $Pb$  and  $Sn$  perovskite segments in the  $(4Tm)_2PbI_4$ – $(4Tm)_2SnI_4$  heterostructure exhibit a slight contrast in the optical image and distinct emission colours in the photoluminescence image (Fig. 4c). The peripheral region exhibits an identical photoluminescence spectrum with the reference  $(4Tm)_2SnI_4$  crystal (Supplementary Fig. 23). Another, smaller, conjugated ligand,  $PEA^+$ , was used to construct a lateral heterostructure between  $Br$  and  $I$  components. As shown in Fig. 4d, the photoluminescence image and spectrum of the  $(PEA)_2PbI_4$ – $(PEA)_2PbBr_4$  heterostructure are close to those of  $(BA)_2PbI_4$ – $(BA)_2PbBr_4$ , showing a purple–blue colour in the centre and green in the peripheral region. In addition, we have created  $(PEA)_2SnI_4$ – $(PEA)_2PbBr_4$  lateral heterostructures based on different halides and different metals at the same time, where the inorganic backbone is  $[PbBr_4]^{2-}$  in the interior region and  $[SnI_4]^{2-}$  in the peripheral region (Fig. 4e).

Apart from the two-segment concentric heterostructures, more complex heterostructures have also been demonstrated. As shown in Fig. 4f, the  $(2T)_2PbI_4$ – $(2T)_2PbBr_4$   $\times n$  ( $n = 2, 3, 4$ ) superlattices are synthesized through multiple repeated growth steps. As indicated in the schematic illustration and the photoluminescence image, 4–8 concentric rectangles are formed, with green emission regions representing

(2T)<sub>2</sub>PbI<sub>4</sub> and quenched regions representing (2T)<sub>2</sub>PbBr<sub>4</sub>. Additionally, multiheterostructures are realized by a third growth of the (2T)<sub>2</sub>SnI<sub>4</sub> layer with a red emission along the (2T)<sub>2</sub>PbI<sub>4</sub>–(2T)<sub>2</sub>PbBr<sub>4</sub> heterostructure (Fig. 4g). Additionally, the synthetic yields of the above-mentioned heterostructures are very high, as illustrated in the lower magnification optical and photoluminescence images (Supplementary Fig. 24). The thickness of the heterostructures ranges from a single cell to a few unit cells, as demonstrated by the AFM study (Supplementary Fig. 25).

## Discussion

These 2D heterostructures exhibit useful optical and electronic properties. For instance, as summarized in Fig. 5a–g<sup>41–43</sup>, the band alignments of these heterostructures can be modulated either by varying the inorganic composition in the lateral in-plane direction or by modifying the molecular structure in the out-of-plane direction. To the best of our knowledge, such multicomplex integrated systems have not previously been realized in other nanoscale heterostructures. To investigate the electronic properties and demonstrate potential device applications of the heterostructures, we have fabricated a proof-of-concept thin-film electrical diode based on a (4Tm)<sub>2</sub>SnI<sub>4</sub>–(4Tm)<sub>2</sub>PbI<sub>4</sub> heterostructure with a type-II band alignment (Fig. 5h). Stable electrical rectifying behaviour with a rectification ratio of around 10<sup>2</sup> was observed without hysteresis. Furthermore, we observed an enhanced exciton lifetime at the interface of the (2T)<sub>2</sub>PbBr<sub>4</sub>–(2T)<sub>2</sub>PbI<sub>4</sub> heterostructure and the (4Tm)<sub>2</sub>SnI<sub>4</sub>–(4Tm)<sub>2</sub>PbI<sub>4</sub> heterostructure from the fluorescence-lifetime imaging measurements, which shed light upon the possibility of tuning the optoelectronic properties via lattice-strain engineering at the interfaces of the heterostructures and superlattices (Supplementary Fig. 26 and Supplementary Table 4).

We have shown that the ion interdiffusion across 2D halide perovskite heterojunctions can be substantially inhibited by using rigid conjugated ligands in the 2D perovskite structure. This suppression of ion migration enables stable and near-atomically sharp interfaces to be obtained via sequential epitaxial growth. The generic synthesis of a wide range of 2D lateral halide perovskite heterostructures, superlattices and multiheterostructures not only presents a powerful platform for advancing the fundamental crystal chemistry of halide perovskites, but also opens up the possibility of further exploring their optoelectronic properties and their applications in diodes, lasers, transistors and photovoltaic devices. Particularly, the role of the conjugated organic ligands on the electronic properties of the heterostructures is worthy of further investigation. More importantly, these findings and methodologies may be extended to other classes of solution-processed 2D nanomaterials.

## Online content

Any methods, additional references, Nature Research reporting summaries, source data, extended data, supplementary information, acknowledgements, peer review information; details of author contributions and competing interests; and statements of data and code availability are available at <https://doi.org/10.1038/s41586-020-2219-7>.

- Lugli, P. & Goodnick, S. M. Nonequilibrium longitudinal-optical phonon effects in GaAs-AlGaAs quantum wells. *Phys. Rev. Lett.* **59**, 716–719 (1987).
- Ahn, C. H., Rabe, K. M. & Triscone, J.-M. Ferroelectricity at the nanoscale: local polarization in oxide thin films and heterostructures. *Science* **303**, 488–491 (2004).
- Bernevig, B. A., Hughes, T. L. & Zhang, S.-C. Quantum spin Hall effect and topological phase transition in HgTe quantum wells. *Science* **314**, 1757–1761 (2006).
- Gong, Y. et al. Vertical and in-plane heterostructures from WS<sub>2</sub>/MoS<sub>2</sub> monolayers. *Nat. Mater.* **13**, 1135–1142 (2014).
- Zhang, Z. et al. Robust epitaxial growth of two-dimensional heterostructures, multiheterostructures, and superlattices. *Science* **357**, 788–792 (2017).
- Sahoo, P. K., Memaran, S., Xin, Y., Balicas, L. & Gutiérrez, H. R. One-pot growth of two-dimensional lateral heterostructures via sequential edge-epitaxy. *Nature* **553**, 63–67 (2018).
- Xie, S. et al. Coherent, atomically thin transition-metal dichalcogenide superlattices with engineered strain. *Science* **359**, 1131–1136 (2018).
- Kojima, A., Teshima, K., Shirai, Y. & Miyasaka, T. Organometal halide perovskites as visible-light sensitizers for photovoltaic cells. *J. Am. Chem. Soc.* **131**, 6050–6051 (2009).
- Tsai, H. et al. High-efficiency two-dimensional Ruddlesden–Popper perovskite solar cells. *Nature* **536**, 312–316 (2016).
- Bai, S. et al. Planar perovskite solar cells with long-term stability using ionic liquid additives. *Nature* **571**, 245–250 (2019).
- Cao, Y. et al. Perovskite light-emitting diodes based on spontaneously formed submicrometre-scale structures. *Nature* **562**, 249–253 (2018).
- Yakunin, S. et al. Detection of X-ray photons by solution-processed lead halide perovskites. *Nat. Photon.* **9**, 444–449 (2015).
- Wei, H. et al. Sensitive X-ray detectors made of methylammonium lead tribromide perovskite single crystals. *Nat. Photon.* **10**, 333–339 (2016).
- Feng, J. et al. Single-crystalline layered metal-halide perovskite nanowires for ultrasensitive photodetectors. *Nat. Electron.* **1**, 404–410 (2018).
- Sutherland, B. R. & Sargent, E. H. Perovskite photonic sources. *Nat. Photon.* **10**, 295–302 (2016).
- Snaith, H. J. Present status and future prospects of perovskite photovoltaics. *Nat. Mater.* **17**, 372–376 (2018).
- Berry, J. et al. Hybrid organic–inorganic perovskites (HOIPs): opportunities and challenges. *Adv. Mater.* **27**, 5102–5112 (2015).
- Akkerman, Q. A. et al. Tuning the optical properties of cesium lead halide perovskite nanocrystals by anion exchange reactions. *J. Am. Chem. Soc.* **137**, 10276–10281 (2015).
- Hoffman, J. B., Lennart Schleper, A. & Kamat, P. V. Transformation of sintered CsPbBr<sub>3</sub> nanocrystals to cubic CsPbI<sub>3</sub> and gradient CsPbBr<sub>x</sub>I<sub>3-x</sub> through halide exchange. *J. Am. Chem. Soc.* **138**, 8603–8611 (2016).
- Lai, M. et al. Intrinsic anion diffusivity in lead halide perovskites is facilitated by a soft lattice. *Proc. Natl. Acad. Sci. USA* **115**, 11929–11934 (2018).
- Pan, D. et al. Visualization and studies of ion-diffusion kinetics in cesium lead bromide perovskite nanowires. *Nano Lett.* **18**, 1807–1813 (2018).
- Park, N.-G., Grätzel, M., Miyasaka, T., Zhu, K. & Emery, K. Towards stable and commercially available perovskite solar cells. *Nat. Energy* **1**, 16152 (2016).
- Rong, Y. et al. Challenges for commercializing perovskite solar cells. *Science* **361**, eaat8235 (2018).
- Park, B. & Seok, S. I. Intrinsic instability of inorganic–organic hybrid halide perovskite materials. *Adv. Mater.* **31**, 1805337 (2019).
- Wang, Z. et al. Efficient ambient-air-stable solar cells with 2D–3D heterostructured butylammonium–caesium–formamidinium lead halide perovskites. *Nat. Energy* **2**, 17135 (2017).
- Huang, Z. et al. Suppressed ion migration in reduced-dimensional perovskites improves operating stability. *ACS Energy Lett.* **4**, 1521–1527 (2019).
- Dou, L. et al. Atomically thin two-dimensional organic–inorganic hybrid perovskites. *Science* **349**, 1518–1521 (2015).
- Jemli, K. et al. Two-dimensional perovskite activation with an organic luminophore. *ACS Appl. Mater. Interfaces* **7**, 21763–21769 (2015).
- Connor, B. A., Leppert, L., Smith, M. D., Neaton, J. B. & Karunadasa, H. I. Layered halide double perovskites: dimensional reduction of Cs<sub>2</sub>AgBiBr<sub>6</sub>. *J. Am. Chem. Soc.* **140**, 5235–5240 (2018).
- Leng, K. et al. Molecularly thin two-dimensional hybrid perovskites with tunable optoelectronic properties due to reversible surface relaxation. *Nat. Mater.* **17**, 908–914 (2018).
- Zhang, Q., Chu, L., Zhou, F., Ji, W. & Eda, G. Excitonic properties of chemically synthesized 2D organic–inorganic hybrid perovskite nanosheets. *Adv. Mater.* **30**, 1704055 (2018).
- Spanopoulos, I. et al. Uniaxial expansion of the 2D Ruddlesden–Popper perovskite family for improved environmental stability. *J. Am. Chem. Soc.* **141**, 5518–5534 (2019).
- Cortecchia, D. et al. Broadband emission in two-dimensional hybrid perovskites: the role of structural deformation. *J. Am. Chem. Soc.* **139**, 39–42 (2017).
- Yang, S. et al. Ultrathin two-dimensional organic–inorganic hybrid perovskite nanosheets with bright, tunable photoluminescence and high stability. *Angew. Chem. Int. Ed.* **56**, 4252–4255 (2017).
- Saparov, B. & Mitzi, D. B. Organic–inorganic perovskites: structural versatility for functional materials design. *Chem. Rev.* **116**, 4558–4596 (2016).
- Ortiz-Cervantes, C. et al. Thousand-fold conductivity increase in 2D perovskites by polydiacetylene incorporation and doping. *Angew. Chem. Int. Ed.* **57**, 13882–13886 (2018).
- Liu, C. et al. Tunable semiconductors: control over carrier states and excitations in layered hybrid organic–inorganic perovskites. *Phys. Rev. Lett.* **121**, 146401 (2018).
- Borg, R. J. & Dienes, G. J. *An Introduction to Solid State Diffusion* (Academic Press, 1988).
- Yu, Y. et al. Atomic resolution imaging of halide perovskites. *Nano Lett.* **16**, 7530–7535 (2016).
- Matthews, J. Defects in epitaxial multilayers I. Misfit dislocations. *J. Cryst. Growth* **27**, 118–125 (1974).
- Gao, Y. et al. Molecular engineering of organic–inorganic hybrid perovskites quantum wells. *Nat. Chem.* **11**, 1151–1157 (2019).
- Gao, Y. et al. Highly stable lead-free perovskite field-effect transistors incorporating linear π-conjugated organic ligands. *J. Am. Chem. Soc.* **141**, 15577–15585 (2019).
- Silver, S., Yin, J., Li, H., Brédas, J. L. & Kahn, A. Characterization of the valence and conduction band levels of  $n=1$  2D perovskites: a combined experimental and theoretical investigation. *Adv. Energy Mater.* **8**, 1703468 (2018).

**Publisher's note** Springer Nature remains neutral with regard to jurisdictional claims in published maps and institutional affiliations.

© The Author(s), under exclusive licence to Springer Nature Limited 2020

## Methods

### Solution-phase synthesis of pure 2D halide perovskite sheets

In this study, ten types of pure 2D halide perovskite sheets were synthesized via a quaternary solvent method.

**Chemicals and reagents.** Organic solvents, including anhydrous chlorobenzene (CB), dimethylformide (DMF), acetonitrile (AN) and dichlorobenzene (DCB) and solid chemicals, including lead bromide ( $\text{PbBr}_2$ ), lead iodide ( $\text{PbI}_2$ ) and tin iodide ( $\text{SnI}_2$ ), were purchased commercially (Sigma Aldrich). *n*-butylammonium bromide (BA·HBr), *n*-butylammonium iodide (BA·HI), phenethylammonium bromide (PEA·HBr) and phenethylammonium iodide (PEA·HI) were purchased commercially (Greatcell Solar). All above chemicals were used as received. Other ammonium salt ligands, including 2T·HI, 2T·HBr, 4Tm·HI and BTm·HI were synthesized in our lab<sup>41</sup>.

**Synthesis of 2D halide perovskite sheets.** 10  $\mu\text{mol}$  of  $\text{MX}_2$  ( $\text{M} = \text{Pb or Sn, X} = \text{Br or I}$ ) and 20  $\mu\text{mol}$  of L·HX ( $\text{L} = \text{BA, PEA, 2T, 4Tm or BTm, X} = \text{Br or I}$ ) were dissolved in 2 ml of DMF/CB co-solvent (1:1 volume ratio) to prepare 5 mM of stock solution. The stock solution was then diluted 120 times by CB/AN/DCB co-solvent (2.5:1:0.01 volume ratio). 5–10  $\mu\text{l}$  of diluted solution was added onto the growth substrate  $\text{SiO}_2$  (300 nm)/Si, which was placed at the bottom of a 4 ml glass vial. The 4 ml vial was then transferred into a secondary glass vial (20 ml) containing 3 ml of CB. After that, the secondary vial was capped and moved onto a 70 °C hot plate. The antisolvent (CB) inside the secondary vial slows down the solvent evaporation from the substrate and facilitates the formation of large 2D halide perovskite sheets. The growth typically took 10–30 min. Solution preparation and sheets growth were carried out in a  $\text{N}_2$ -filled glovebox. The growth substrate was cleaned in piranha acid for 2 h before use.

The growth steps for all the halide perovskite sheets in Supplementary Fig. 22 were the same. However, the growth parameters for some sheets were slightly different. The above recipe applies to the growth of  $(2\text{T})_2\text{PbBr}_4$ ,  $(\text{BA})_2\text{PbBr}_4$ ,  $(\text{BA})_2\text{PbI}_4$  and  $(\text{PEA})_2\text{PbBr}_4$ . For  $(2\text{T})_2\text{PbI}_4$ ,  $(2\text{T})_2\text{SnI}_4$  and  $(\text{PEA})_2\text{PbI}_4$ , the stock solution was diluted 120 times by CB/AN/DCB co-solvent (9.5:1:0.01 volume ratio). For  $(4\text{Tm})_2\text{PbI}_4$  and  $(4\text{Tm})_2\text{SnI}_4$ , the stock solution was diluted 240 times by CB/AN/DCB co-solvent (3.9:1:0.01 volume ratio) and the growth temperature was 90 °C. For  $(\text{BTm})_2\text{PbI}_4$ , the stock solution was diluted 1,440 times by CB/AN/DCB co-solvent (7.4:1:0.01 volume ratio) and the growth temperature was 90 °C.

For the quaternary solvent method for crystal growth, CB helps reduce the solubility of 2D perovskite in DMF and promotes the sheet crystallization. AN has a lower boiling point compared to CB, and 2D perovskite has a limited solubility in AN. In this case, AN evaporates more quickly and initiates the 2D perovskite nucleation at a relatively low concentration, thus decreasing the thickness of sheets. Moreover, compared to CB, DCB has a higher boiling point. The addition of DCB avoids the gradually increasing concentration of perovskite solution with the evaporation of AN and CB, thus ensuring the uniform distribution of sheets throughout the growth substrate.

### Epitaxial synthesis of 2D lateral halide perovskite heterostructures

The epitaxial growth of 2D lateral halide perovskite heterostructures was based on the above quaternary solvent method. The growth of the first sheet is identical to above method. To eliminate the possibility of crystal damage, subsequent growth was performed under milder growth conditions in our study—that is, by lowering the growth temperature or adding more antisolvent in the solution.

**$(2\text{T})_2\text{PbI}_4$ – $(2\text{T})_2\text{PbBr}_4$  heterostructures and superlattices.** The sequence of the two steps for heterostructure formation (Br followed

by I versus I followed by Br) is dictated by the solubility difference of the two halide perovskites in the solvent system. As  $(2\text{T})_2\text{PbBr}_4$  has a lower solubility in the quaternary solvent, it is synthesized before  $(2\text{T})_2\text{PbI}_4$ . The  $(2\text{T})_2\text{PbI}_4$  stock solution was diluted 480 times by CB/AN/DCB co-solvent (6:1:0.01 volume ratio) for the growth of heterostructures. After the growth of  $(2\text{T})_2\text{PbBr}_4$  sheets, the hot plate was cooled down to 50 °C. Then 10  $\mu\text{l}$  of the diluted  $(2\text{T})_2\text{PbI}_4$  solution was added onto the growth substrate. The epitaxial growth of  $(2\text{T})_2\text{PbI}_4$  along the  $(2\text{T})_2\text{PbBr}_4$  sheets typically took about 30 min. The  $(2\text{T})_2\text{PbI}_4$ – $(2\text{T})_2\text{PbBr}_4$   $\times n$  superlattices were realized by  $n$  repeated growths of  $(2\text{T})_2\text{PbI}_4$ – $(2\text{T})_2\text{PbBr}_4$  heterostructures.

**$(\text{BA})_2\text{PbI}_4$ – $(\text{BA})_2\text{PbBr}_4$  heterostructures.** The  $(\text{BA})_2\text{PbI}_4$  stock solution was diluted 240 times by CB/AN/DCB co-solvent (6:1:0.01 volume ratio) for the growth of heterostructures. After the growth of the  $(\text{BA})_2\text{PbBr}_4$  sheets, the hot plate was cooled down to 50 °C. Then 10  $\mu\text{l}$  of the diluted  $(\text{BA})_2\text{PbI}_4$  solution was added onto the growth substrate. The epitaxial growth of  $(\text{BA})_2\text{PbI}_4$  along  $(\text{BA})_2\text{PbBr}_4$  sheets typically took about 30 min.

**$(\text{BTm})_2\text{PbI}_4$ – $(4\text{Tm})_2\text{PbI}_4$  heterostructures.** The  $(\text{BTm})_2\text{PbI}_4$  stock solution was diluted 1,440 times by CB/AN/DCB co-solvent (3.2:1:0.01 volume ratio) for the growth of heterostructures. After the growth of the  $(4\text{Tm})_2\text{PbI}_4$  sheets, the hot plate was cooled down to 50 °C. Then 10  $\mu\text{l}$  of the diluted  $(\text{BTm})_2\text{PbI}_4$  solution was added onto the growth substrate. The epitaxial growth of  $(\text{BTm})_2\text{PbI}_4$  along  $(4\text{Tm})_2\text{PbI}_4$  sheets typically took about 30 min.

**$(2\text{T})_2\text{SnI}_4$ – $(2\text{T})_2\text{PbI}_4$  heterostructures.** The  $(2\text{T})_2\text{SnI}_4$  stock solution was diluted 120 times by CB/AN/DCB co-solvent (9.5:1:0.01 volume ratio) for the growth of heterostructures. After the growth of the  $(2\text{T})_2\text{PbI}_4$  sheets, the hot plate was cooled down to 50 °C. Then 10  $\mu\text{l}$  of the diluted  $(2\text{T})_2\text{SnI}_4$  solution was added onto the growth substrate. The epitaxial growth of  $(2\text{T})_2\text{SnI}_4$  along the  $(2\text{T})_2\text{PbI}_4$  sheets typically took about 30 min.

**$(4\text{Tm})_2\text{SnI}_4$ – $(4\text{Tm})_2\text{PbI}_4$  heterostructures.** The  $(4\text{Tm})_2\text{SnI}_4$  stock solution was diluted 240 times by CB/AN/DCB co-solvent (1.8:1:0.01 volume ratio) for the growth of heterostructures. After the growth of the  $(4\text{Tm})_2\text{PbI}_4$  sheets, the hot plate was cooled down to 80 °C. Then 10  $\mu\text{l}$  of the diluted  $(4\text{Tm})_2\text{SnI}_4$  solution was added onto the growth substrate. The epitaxial growth of  $(4\text{Tm})_2\text{SnI}_4$  along the  $(4\text{Tm})_2\text{PbI}_4$  sheets typically took about 10 min.

**$(\text{PEA})_2\text{PbI}_4$ – $(\text{PEA})_2\text{PbBr}_4$  heterostructures.** The  $(\text{PEA})_2\text{PbI}_4$  stock solution was diluted 240 times by CB/AN/DCB co-solvent (9.5:1:0.01 volume ratio) for the growth of heterostructures. After the growth of the  $(\text{PEA})_2\text{PbBr}_4$  sheets, the hot plate was cooled down to 50 °C. Then 10  $\mu\text{l}$  of the diluted  $(\text{PEA})_2\text{PbI}_4$  solution was added onto the growth substrate. The epitaxial growth of  $(\text{PEA})_2\text{PbI}_4$  along the  $(\text{PEA})_2\text{PbBr}_4$  sheets typically took about 30 min.

**$(\text{PEA})_2\text{SnI}_4$ – $(\text{PEA})_2\text{PbBr}_4$  heterostructures.** The  $(\text{PEA})_2\text{SnI}_4$  stock solution was diluted 580 times by CB/AN/DCB co-solvent (35:2:0.01 volume ratio) for the growth of heterostructures. After the growth of the  $(\text{PEA})_2\text{PbBr}_4$  sheets, the hot plate was cooled down to 50 °C. Then 10  $\mu\text{l}$  of the diluted  $(\text{PEA})_2\text{SnI}_4$  solution was added onto the growth substrate. The epitaxial growth of  $(\text{PEA})_2\text{PbI}_4$  along  $(\text{PEA})_2\text{PbBr}_4$  sheets typically took about 30 min.

**$(2\text{T})_2\text{SnI}_4$ – $(2\text{T})_2\text{PbI}_4$ – $(2\text{T})_2\text{PbBr}_4$  multiheterostructures.**  $(2\text{T})_2\text{SnI}_4$  stock solution was diluted 480 times by CB/AN/DCB co-solvent (9.5:1:0.01 volume ratio) for the growth of multiheterostructures. Following the growth of the  $(2\text{T})_2\text{PbI}_4$ – $(2\text{T})_2\text{PbBr}_4$  heterostructures, 10  $\mu\text{l}$  of the diluted  $(2\text{T})_2\text{SnI}_4$  solution was added onto the growth substrate. The epitaxial

# Article

growth of  $(2T)_2SnI_4$  along the  $(2T)_2PbI_4$  sheets typically took about 30 min. The growth temperature was set at 50 °C.

**One-pot synthesis of  $(2T)_2PbI_4$ – $(2T)_2PbBr_4$  heterostructures.** The  $(2T)_2PbI_4$  and  $(2T)_2PbBr_4$  stock solutions were mixed in a 1:1 ratio and diluted 480 times by CB/AN/DCB co-solvent (6:1:0.01 volume ratio) for the one-pot growth of heterostructures. 10 µl of the diluted solution was added onto the growth substrate at a temperature of 70 °C. The Br and I components phase-separated spontaneously during the evaporation of the solvents. The coherent epitaxial growth of  $(2T)_2PbI_4$  along the  $(2T)_2PbBr_4$  sheets typically took about 10 min.

**$(4Tm)_2SnI_4$ – $(4Tm)_2PbI_4$  thin film lateral heterostructure devices.**  $(4Tm)_2PbI_4$  (0.1 mol l<sup>-1</sup>) was spin-coated on insulating substrates (quartz or SiO<sub>2</sub>/Si), followed by 180 °C annealing on a hot plate for 5 min. Then, half of the  $(4Tm)_2PbI_4$  film was removed by razor blade, and the rest of the film was covered by a Kapton tape. The sample was then treated by ultraviolet ozone for 30–60 min to make the exposed area hydrophilic. The Kapton tape was removed and  $(4Tm)_2SnI_4$  (0.1 mol l<sup>-1</sup>) was spin-coated on the ultraviolet ozone-treated sample, followed by 175 °C annealing for 5 min. Finally, silver wire (diameter, 120 µm) was placed at the interface region, serving as the shadow mask for Au evaporation. 50-nm Au was evaporated as the electrodes.

## Characterizations

**Optical imaging.** The bright-field optical images were collected by a custom microscope (Olympus BX53).

**Photoluminescence imaging and spectra collection.** Samples were excited with a light source (012-63000; X-CITE 120 REPL LAMP). The filter cube contains a bandpass filter (330–385 nm) for excitation, and a dichroic mirror (cutoff wavelength, 400 nm) for light splitting and a filter (long pass 420 nm) for emission. The photoluminescence spectra were collected by a spectrometer (SpectraPro HRS-300).

**Interdiffusion calculation.** We used a simplified one-dimensional diffusion model of Fick's second law to describe the transient concentration profile across the lateral heterostructures. The model is mathematically expressed as  $\frac{\partial C}{\partial t} = \frac{\partial}{\partial x} \left( D(c) \frac{\partial C}{\partial x} \right)$ . Here,  $C$  is the concentration of Br,  $t$  is the heating time,  $x$  is the length and  $D$  is the inter-diffusion coefficient of halides. The diffusion coefficient is calculated using the classical Boltzmann–Matano method. The evolution of the concentration profile for the BA and 2T lateral heterostructures is fitted by a normal cumulative distribution function,  $y = y_0 + A \int_{-\infty}^x \frac{1}{\sqrt{2\pi}w} \exp\left(-\frac{(t-x_0)^2}{2w^2}\right) dt$ . The fitted curves, along with the experimental Br concentration obtained from the photoluminescence emission peaks, are shown in Supplementary Fig. 7. We note that the concentration profile obtained using the edge widths and photoluminescence emissions can only be used for a rough estimation of the diffusion coefficients because no gradient is assumed across the overlaid edge widths of the lateral heterostructures. It is estimated that the diffusion coefficient of the  $(BA)_2PbI_4$ – $(BA)_2PbBr_4$  and  $(2T)_2PbI_4$ – $(2T)_2PbBr_4$  lateral heterostructures are of the order of approximately  $10^{-13}$  cm<sup>2</sup> s<sup>-1</sup> to  $10^{-12}$  cm<sup>2</sup> s<sup>-1</sup> and approximately  $10^{-16}$  cm<sup>2</sup> s<sup>-1</sup> to  $10^{-15}$  cm<sup>2</sup> s<sup>-1</sup>, respectively.

**SEM imaging.** The backscattering SEM images were collected by a scanning electron microscope (FEI TeneoVS). The acceleration voltage was 1 kV and the acceleration current was 0.1 nA.

**Powder XRD measurements.** Powder XRD was measured using a powder X-ray diffractometer (Panalytical Empyrean) with a Cu K $\alpha$  source.

**AFM.** AFM images were recorded in tapping mode using an atomic force microscope (Bruker MultiMode 8).

**Fluorescence-lifetime imaging microscopy measurements.** The samples with PMMA (950 PMMA A4, Microchem) coating were measured with a 50 × 0.55 numerical aperture air objective in a confocal laser scanning microscope (LSM 510 NLO AxioVert200M) equipped with a tunable laser (Mai-Tai HP). The excitation wavelength was 405 nm, from the second harmonic of 810 nm (<100 fs, 80 MHz). Lifetime measurements were performed using time-correlated single photon counting (Becker-Hickl SPC-150). The lifetime decay was collected and analysed using Becker-Hickl SPCM software.

**Single-crystal XRD measurement.** Single crystals of  $(2T)_2PbBr_4$  were analysed using a diffractometer (Bruker Quest) with kappa geometry, an I-µ-S microsource X-ray tube, a laterally graded multilayer Göbel mirror single crystal for monochromatization, an area detector (Photon2 CMOS) and a low-temperature device (Oxford Cryosystems). Examination and data collection were performed with Cu K $\alpha$  radiation ( $\lambda = 1.54178$  Å) at 150 K.

**Electric measurement.** Current–voltage characteristics were acquired by sweeping the bias voltages from -10 V to 10 V and then from 10 V to -10 V based on a probe station (PS100 Lakeshore) with a source meter (Keithley 2400).

## TEM characterizations

**TEM sample preparation of pure  $(2T)_2PbI_4$ ,  $(2T)_2PbBr_4$  sheets and  $(2T)_2PbI_4$ – $(2T)_2PbBr_4$  heterostructure.** To transfer pure  $(2T)_2PbI_4$ ,  $(2T)_2PbBr_4$  sheets or  $(2T)_2PbI_4$ – $(2T)_2PbBr_4$  heterostructures to the TEM grids, a layer of PMMA was spin-coated on the growth SiO<sub>2</sub>/Si substrates before perovskite growth. The spin-coating speed was 3,000 rpm and the duration time was 1 min. Then the Si substrates were placed on a 70 °C hot plate for 10 min to condense the PMMA and remove the residue solvent. After that, the perovskites were grown on the PMMA-coated Si.

The transfer process of perovskites from the growth PMMA/Si substrates was performed in the glove box. First, the growth substrates were dipped into CB to dissolve the sacrificial layer PMMA, which facilitates the detachment of samples from the growth substrates. Then, vortex mixing or ultrasonication was used to further detach the samples from Si substrates. Afterwards, the suspension was dropped onto the TEM grids. TEM grids were rinsed with clean CB a few times to remove the residue PMMA. The TEM grids (Lacey/carbon grids on 200-mesh Cu, Ted Pella) were covered by one layer of carbon-nanotube film and mono-layer graphene hybrids to mitigate electron-beam damage.

**TEM imaging and spectrum acquisition.** The diffraction patterns were obtained on a 200-kV transmission electron microscope (JEOL JEM-2100plus) with a camera (TEMCam-XF416, TVIPS). The AC-HRTEM and EDS mapping was taken on an 80-kV aberration-corrected transmission electron microscope (JEOL GrandARM) equipped with a fast camera (OneView IS, Gatan). The EDS map is an intensity map based on X-ray counts, which are proportional to the content of the element. A low accelerating voltage was used to enhance the contrast at low magnifications when searching for samples and locating the interface positions. The low-dose-rate imaging was achieved by increasing electron-beam spot size (decreasing the beam current) and reducing the brightness of the electron beam (spreading the beam illumination). To avoid unnecessary electron-beam damage, the minimum-dose system was used to reduce damage while searching for the samples and during focusing.

There are usually minor displacements between continuously captured images due to the mechanical vibration of the specimen holder

and the effect of electron irradiation; if we were to simply superpose these images, it would lower the spatial resolution of the HRTEM image. To correct these displacement drifts, we use a digital micrograph script developed by D. R. G. Mitchell ([http://www.dmscripting.com/stack\\_alignment.html](http://www.dmscripting.com/stack_alignment.html)). The core of the script is to measure the drift by cross-correlation, thus applying measured drift to each image. Each drift measurement will produce a cross correlation value, which is a guide to whether it is working well ('1' is good, '0.5' is OK). In our case, the cross-correlation values are 0.644, 0.645 and 0.647 when processing the four raw images. After accurate drift alignment, the images can be superposed to produce a HRTEM image with an improved signal-to-noise ratio.

**TEM simulation and structural model.** The kinematical SAED patterns were simulated with the MacTempasX<sup>44</sup> software. The structural models were constructed with the VESTA 3D visualization program<sup>45</sup>.

### Molecular dynamics simulations

For the molecular dynamics simulation of the heterojunction between Pb–Br and Pb–I organic–inorganic perovskites, the MYP model for hybrid perovskites was used<sup>46–48</sup>. The MYP model was originally developed for Pb–I perovskites and has been extended to Pb–Br perovskites. It treats the organic–organic interactions by the standard assisted model building with energy refinement (AMBER) force fields, the inorganic–inorganic interactions between Pb, I and Br by Buckingham potentials, and the organic–inorganic interactions as the sum of Buckingham, electrostatic and Lennard–Jones 12–6 terms. As developed and reported, the charges on the metal, halide and cation are non-integer. For our simulations, we employed integer values for these charges; the MYP non-bonded parameters were appropriately rescaled to reproduce the cohesive energy density of the unscaled simulation.

The surface cation geometries were optimized using the program ORCA<sup>49</sup> with the  $\omega$ B97X-D<sup>50</sup>/def2-TVZP<sup>51,52</sup> density functional theory (DFT) potentials. The standard general AMBER force field (GAFF) parameterization was used for the organic cations<sup>53</sup>, and the cation point charges were fit against the electrostatic DFT potential ( $\omega$ B97X-D/def2-TVZP) of the isolated cation with a +1 charge. The molecular dynamics software LAMMPS was used for the molecular simulations<sup>54</sup>. All simulations used a 1 fs integration timestep and periodic boundary conditions. The particle–particle–particle–mesh (PPPM) algorithm was used for the long-range electrostatics, and Lennard–Jones interactions were truncated at 15 Å. Following the MYP model, the 1–4 pairwise Lennard–Jones interactions were scaled by 0.5 and the 1–4 electrostatics interactions were scaled by 0.833. A sample LAMMPS input file with all force-field parameters is supplied in Supplementary Data.

The initial perovskite heterojunction geometry was generated by constructing an ideal perovskite monolayer composed of two domains: a  $6 \times 1 \times 12$  Pb–I domain and a  $6 \times 1 \times 12$  Pb–Br domain, for a total system size of  $12 \times 1 \times 12$  of  $A_2BX_4$  unit cells. Halide vacancies were introduced by randomly removing two halide atoms. The simulation was first relaxed under the NVE ensemble for 50 ps with restrained atomic displacements of 0.01 Å per timestep. The system was then simulated for 20 ns with the Nosé–Hoover thermostat and barostat, with the barostat applied only to the x and z directions (which define the plane of the perovskite), to allow the surface cations and halides to be displaced from the perovskite layer, at both 298 K and 800 K. To calculate the free energy required to remove a surface cation and halide, a  $6 \times 1 \times 6$ -unit-cell simulation

on pristine (that is, no vacancies) Pb–Br and Pb–I perovskites was run, with a surface cation and a halide atom displaced from their initial positions out to vacuum in 0.5 Å intervals. The system was equilibrated for 0.5 ns and then simulated for 10 ns under the NVT ensemble at 298 K for each displacement. The *pymbar* package was used to calculate the free energies<sup>55</sup>.

### Data availability

All data related to this study are available from the corresponding author on reasonable request.

44. O’Keefe, M. A. & Kilaas, R. *Advances in High-resolution Image Simulation*. Report no. LBL-24727 (Lawrence Berkley National Laboratory, 1988); <https://escholarship.org/uc/item/6qb303ch>.
45. Momma, K. & Izumi, F. VESTA 3 for three-dimensional visualization of crystal, volumetric and morphology data. *J. Appl. Cryst.* **44**, 1272–1276 (2011).
46. Mattoni, A., Filippetti, A., Saba, M. I. & Delugas, P. Methylammonium rotational dynamics in lead halide perovskite by classical molecular dynamics: the role of temperature. *J. Phys. Chem. C* **119**, 17421–17428 (2015).
47. Mattoni, A., Filippetti, A. & Caddeo, C. Modeling hybrid perovskites by molecular dynamics. *J. Phys. Condens. Matter* **29**, 043001 (2017).
48. Hata, T., Giorgi, G., Yamashita, K., Caddeo, C. & Mattoni, A. Development of a classical interatomic potential for MAPbBr<sub>3</sub>. *J. Phys. Chem. C* **121**, 3724–3733 (2017).
49. Neese, F. The ORCA program system. *Wiley Interdiscip. Rev. Comput. Mol. Sci.* **2**, 73–78 (2012).
50. Chai, J.-D. & Head-Gordon, M. Long-range corrected hybrid density functionals with damped atom–atom dispersion corrections. *Phys. Chem. Chem. Phys.* **10**, 6615–6620 (2008).
51. Schäfer, A., Horn, H. & Ahlrichs, R. Fully optimized contracted Gaussian basis sets for atoms Li to Kr. *J. Chem. Phys.* **97**, 2571–2577 (1992).
52. Weigend, F. & Ahlrichs, R. Balanced basis sets of split valence, triple zeta valence and quadruple zeta valence quality for H to Rn: design and assessment of accuracy. *Phys. Chem. Chem. Phys.* **7**, 3297–3305 (2005).
53. Wang, J., Wolf, R. M., Caldwell, J. W., Kollman, P. A. & Case, D. A. Development and testing of a general AMBER force field. *J. Comput. Chem.* **25**, 1157–1174 (2004).
54. Plimpton, S. Fast parallel algorithms for short-range molecular dynamics. *J. Comput. Phys.* **117**, 1–19 (1995).
55. Shirts, M. R. & Chodera, J. D. Statistically optimal analysis of samples from multiple equilibrium states. *J. Chem. Phys.* **129**, 124105 (2008).

**Acknowledgements** This work is supported by the Office of Naval Research (grant no. N00014-19-1-2296, programme managers P. Armistead and J. Parker), the National Science Foundation (grant no. 1939986-ECCS, programme manager P. Lane), and at Purdue University, the Davidson School of Chemical Engineering, College of Engineering, and the Birck Nanotechnology Center. TEM work is supported by funding from the National Science Foundation of China (grant no. 21805184), the National Science Foundation Shanghai (grant no. 18ZR1425200) and the Center for High-resolution Electron Microscopy (ChEM) at ShanghaiTech University (grant no. EMO2161943). P.Y. acknowledges support from the US Department of Energy, Office of Basic Energy Sciences, Materials Sciences and Engineering Division, under contract no. DE-AC02-05CH11231. J.K. acknowledges support from the Air Force Office of Scientific Research (FATE MURI, grant no. FA9550-15-1-0514). B.M.S. acknowledges support from the Air Force Office of Scientific Research (grant no. FA9550-18-S-0003, programme manager K. Caster). We thank L. Huang, B. Boudouris and S. Li for discussions.

**Author contributions** E.S. synthesized and characterized the 2D perovskite materials; B.Y. and Y.Y. performed TEM characterization and data analysis; S.B.S. and B.M.S. performed molecular dynamics simulations and data analysis; Y. Gao performed organic ligand synthesis; A., Y. Guo, C.S., M.L., P.Y. and J.K. participated in materials characterization and data analysis; E.S. and L.D. wrote the manuscript; all authors read and revised the manuscript.

**Competing interests** The authors declare no competing interests.

### Additional information

**Supplementary information** is available for this paper at <https://doi.org/10.1038/s41586-020-2219-7>.

**Correspondence and requests for materials** should be addressed to B.M.S., Y.Y. or L.D.

**Peer review information** *Nature* thanks Humberto Gutierrez, Hua Zhang and the other, anonymous, reviewer(s) for their contribution to the peer review of this work.

**Reprints and permissions information** is available at <http://www.nature.com/reprints>.